Title

Multi-modal sensing using photoactive thin films

Journal

Smart Materials and Structures, 23(8)

ISSN

0964-1726

Authors

Ryu, Donghyeon

Loh, Kenneth J

Publication Date

2014-08-01

DOI

10.1088/0964-1726/23/8/085011

Peer reviewed

Multi-modal Sensing using Photoactive Thin Films

Donghyeon Ryu[1] and Kenneth J Loh[1,*]

[1] Department of Civil & Environmental Engineering, University of California, Davis, CA, 95616, U.S.A

[*]Corresponding E-mail: kjloh@ucdavis.edu

Abstract. The need for reliable prognosis of the health of structural systems has promoted the development of sensing technologies capable of simultaneously detecting multiple types of damage. However, conventional sensors are designed to only measure a specific structural response (*e.g.*, strain, displacement, or acceleration). This limitation forces one to use a wide variety of sensors densely instrumented on a given structure, which results in high overhead costs and requires extensive signal processing of sensor raw data. In this study, a photoactive thin film that has been engineered for multi-modal sensing to selectively detect strain and pH is proposed. In addition, the thin film is self-sensing in that it does not require external power to operate. Instead, light illumination causes the photoactive film to generate an electrical current, whose magnitude is directly related to applied strains (for deformations, impact, or cracks) or pH (as a precursor of corrosion). First, the thin films were fabricated by spin-coating photoactive and conjugated polymers like poly(3-hexylthiophene) (P3HT). The thin film was also encoded with pH sensitivity by integrating polyaniline (PANI) as one component within the multi-layered film architecture. Second, the optical response of the P3HT and PANI thin films subjected to applied strains or pH was characterized using absorption spectroscopy. Lastly, it was also verified that the thin films could selectively sense strain or pH depending on the wavelengths of light used for sensor interrogation.

1. Introduction

Over the last few decades, numerous catastrophic incidents involving civil infrastructure, aircraft, naval vessels, and other structural systems have occurred [1-4]. These sudden structural failures have caused severe socioeconomic losses. For example, a natural gas pipeline exploded in Carlsbad, New Mexico in 2000, which resulted in the loss of 12 lives, three vehicles, and ~$1 million due to losses and damage [5]. Internal corrosion, along with the combined effects of moisture, contaminants, and microbes that produced corrosive compounds, caused significant reductions in the steel pipes' thickness. The deteriorated steel pipes were unable to withstand the gas pressure and ruptured [5]. Another example was the 1988 Aloha Airlines flight 243 accident that brought airliner safety to public attention. The upper-front section of the plane's fuselage ripped open and was blown off during flight. It was determined that a lap joint connecting the upper and lower walls of the fuselage was damaged by fatigue cracks around the bolts and was accelerated by crevice corrosion to cause this failure [3]. These examples have demonstrated that catastrophic structural failure can occur suddenly and without any warning. Therefore, there is an urgent need for developing structural health monitoring (SHM) methods that could aid in the detection of different modes of damage that could occur in a given structure and environment.

To detect the onset and propagation of cracks in a timely manner, extensive efforts were made by many researchers using ultrasonics, eddy current sensors, wireless sensor networks, fiber Bragg gratings, non-contact strain sensing, and imaging techniques [6-13]. Achenbach [6] provided an extensive review

of quantitative nondestructive evaluation using ultrasonic sensing techniques for reliable detection of cracks. The review showed how ultrasonics could be integrated with reliable measurement models to evaluate structural integrity via probability analysis and flaw characterization. An eddy current sensing system was developed specifically for detecting fatigue cracks around bolt-hole connections in multiple layers of metallic airframes [7]. On the other hand, Rakow and Chang [7] suggested micro-fabricated conformable sensors, which could wrap around the fastener shank. The sensing unit was integrated with a metallic sleeve to detect cracks beginning near the bolt-hole boundaries. In contrast to other surface-mounted sensors, the main advantage was that this sensing system could capture crack growth and propagation through the depth of the connection holes. However, eddy current-based sensing is limited to non-conductive materials. Xu and Huang [8] employed wireless antennas for tracking sub-millimeter cracks at multiple sites. Two sets of dual antennas were multiplexed for detecting multiple cracks at different locations, where each antenna was operated at different frequencies.

Besides crack sensing, the detection of corrosion is difficult due to its complex electrochemistry and mechanism of formation. A simple laboratory corrosion test is to measure the change in mass of the structural component being studied. However, applying this method to a real structural system is challenging. Instead, most field-based methods monitor corrosion by tracking changes in the structure's properties, such as thickness, conductivity, and permeability, among many others. He *et al.* [14] used a pulsed eddy current system to characterize atmospheric corrosion of mild steel specimens for up to 10 months. The pulsed eddy current effectively tracked changes in electrical conductivity and permeability of mild steel as it corroded. It was found that the electromagnetic properties varied with increased corrosion area and depth. In addition, piezoelectric wafer active sensors that generated and measured Lamb waves were shown to monitor corrosion on aluminum plates [15]. The properties of Lamb waves propagating over the corroded area were affected by changes in plate thickness. Besides active sensing techniques, pH sensors were widely utilized for corrosion sensing, since pH is an important and sensitive indicator of corrosion in metallic structures. Steel used for concrete reinforcement and structural supports is especially vulnerable to corrosion at low pH levels. As pH decreased, the concentration of hydrogen ions (H^+) increased exponentially to cause oxidation (*i.e.*, corrosion). Various types of pH sensors were developed and tested, such as piezoresistive, potentiometric, and optical sensors [16-24]. In particular, polyaniline (PANI) conjugated polymers were one of the most popular materials for developing new thin film pH sensors due to their intrinsic optoelectronic properties, which varied depending on pH [16, 18, 19, 22, 23, 25].

Despite these advancements, it remains challenging to evaluate structural integrity by monitoring just one type of damage mechanism. SHM of simultaneous but different types of damage (*e.g.*, strain/cracks and pH/corrosion) requires the simultaneous use of a multitude of sensors. However, the dense instrumentation of different types of sensors can amount to high overhead costs, and the vast amount of data generated can be difficult to manage. In addition, certain structures (*e.g.*, spacecraft, unmanned aerial vehicles, and other high-value assets) have limited payload and cannot accommodate this SHM methodology. Instead, sensors that could detect multiple types of damage, preferably at the same time, are needed. An example is the recent development of multifunctional materials assembled using carbon nanotubes (CNT), and they have demonstrated the ability to sense different damage features [26, 27]. Specifically, Loh *et al.* [26] showed that the electrical properties of layer-by-layer (LbL) CNT-based thin film sensors varied with changes in strain and pH. While an advantage was that the film's resistance exhibited high sensitivity to strain and pH, there was no explicit way to discriminate the two

effects (particularly, if strain and pH were occurring simultaneously). This limitation made it difficult for monitoring different damage phenomena occurring in a structure, and the need for advances in multi-modal sensing remains.

To overcome the drawbacks of current sensing technologies, Ryu and Loh [28] proposed a new type of strain sensor fabricated using a photoactive poly(3-hexylthiophene) (P3HT) conjugated polymer and CNTs. The photoactive and conformable nanocomposites generated direct current (DC) due to light illumination, and the level of current also varied with applied strains, thus making them multifunctional. While DC photocurrent generation was due to the photovoltaic effect, it was crucial to discover that photocurrent magnitude was directly correlated to the magnitude of strain. Strain sensing was validated up to 5,000 με or 0.5%, and the gage factor was calculated to be ~4.3 and ~7.5 for films with and without CNTs, respectively [28]. Then, it was found that variations in the nanocomposite's light absorption properties contributed to its optoelectronic strain sensing response [29].

This study builds on the aforementioned work and aims to develop a multi-modal, photoactive, and self-sensing thin film that could provide enhanced selectivity for measuring both strain and pH. A multilayered film architecture is proposed, and the basis for photocurrent-based sensing was by spin-coating p-type P3HT and n-type [6,6]-phenyl C61 butyric acid methyl ester (PCBM) to form a p-n bulk heterojunction (BHJ) layer [30, 31]. This P3HT:PCBM layer was responsible for generating DC photocurrent when broadband light was shined on it. Two functional materials, namely P3HT and PANI, enabled multi-modal sensing. The choice of using these two conjugated polymers was because both of them possessed unique optical absorption/transmission properties that were sensitive to strain and pH. First, it was shown that P3HT's linearity and alignment were affected by mechanical deformation, and thus, its strain-induced π-electron delocalization could alter optoelectronic properties [29, 32, 33]. P3HT's extraordinary optoelectronic property was the basis for strain sensing as demonstrated by Ryu and Loh [28]. Second, PANI intrigued many researchers, since its electronic properties, color, and optical transmission were sensitive to pH [16, 19, 22, 23, 25]. In particular, the optical properties of PANI were affected by its oxidation state, which resulted in π-orbital electron delocalization after being exposed to different pH buffer solutions [32, 34].

This paper begins with an overview of the spin-coating and processing procedures employed for fabricating P3HT:PCBM films. Second, the fabrication of the PANI-based pH sensing layer using layer-by-layer self-assembly is explained. Next, using ultraviolet visible (UV-Vis) absorption spectroscopy, the light absorption and transmission properties of the P3HT- and PANI-based layers, as well as how they respond to strain and pH, have been investigated, respectively. These results provide insight as to how their strain and pH sensitivities change with respect to the range of wavelengths of light used for interrogation. Then, after selecting the appropriate light wavelengths, the film's photocurrent generation properties have been characterized and are discussed. Finally, multi-modal and selective sensing of strain and pH are demonstrated (*i.e.*, using blue and infrared light, respectively).

2. Materials and Film Fabrication

2.1. Materials

P3HT (M_W ~60,000; >93% regioregularity) and PCBM (99.5% purity) were purchased from Solaris Chem. Poly(3,4-ethylenedioxythiophene):poly(styrenesulfonate), or PEDOT:PSS, was acquired from Heraeus, and it was used as received. PANI emeraldine base (M_W ~65,000) and poly(sodium 4-styrenesulfonate) (PSS; M_W ~1,000,000) were from Sigma-Aldrich. Indium-tin-oxide (ITO)-coated polyethylene terephthalate (PET) sheets with a sheet resistance of ~6 Ω/sq were from Xinyan Tech. It should be noted that its light transmittance at 550 nm is ~60%. Polydimethylsiloxane (PDMS) was obtained from Dow Corning. All solvents and glassware used were purchased from Fisher Scientific.

2.2. Preparation of Solutions

Two different types of solutions were prepared and used to deposit functional layers, as part of a multilayered thin film architecture, for sensing strain and pH. First, a P3HT-based solution was prepared by dissolving P3HT and PCBM in either dichlorobenzene (DCB) or chlorobenzene (CB); they are referred to as the PP-D or PP-C solution, respectively. As mentioned earlier, P3HT was one of the primary constituents that enabled photocurrent generation and strain sensing. The other solution used for achieving pH sensitivity was obtained by dissolving PANI emeraldine base in dimethylformamide (DMF). This section describes the procedures followed to prepare these solutions.

A total of six different sets of PP-D or PP-C solutions were prepared. Each sample set was characterized by a unique mixing ratio of P3HT and PCBM, numbered from #1 to #6, as shown in table 1. In all six solution sets, the P3HT concentration was fixed at 1 *w/v*%, while PCBM concentration varied from 0.25 to 1.50 *w/v*% and in 0.25 *w/v*% increment. Each solution (*e.g.*, the #5 set as shown in table 1) was obtained by first weighing 100 mg of P3HT and 125 mg of PCBM. Second, P3HT and PCBM powder were combined and dissolved in 10 mL of DCB or CB to obtain a 2.25 *w/v*% solution at a 1.00:1.25 P3HT:PCBM mixing ratio. Complete dissolution was obtained by stirring using a magnetic stir bar and heating at 45 ºC for 24 h. Lastly, the solution was cooled to room temperature and then filtered through a 0.45 μm filter membrane for eliminating any agglomerated particles. All the other five solution sets were prepared by following a similar procedure but with different amounts of PCBM.

The preparation of the 1 *w/v*% PANI solution began with dissolving 100 mg of PANI in 10 mL of DMF. The mixture was stirred on a hot plate/stirrer at 35 ºC for 48 h. After the PANI solution cooled to room temperature, it was filtered using a 0.45 μm membrane, similar to the P3HT:PCBM case. Then, several drops of 10 *v*% hydrochloric acid (HCl) were pipetted to the filtered PANI solution such that its pH was ~2.5. Doping PANI with HCl promoted the conversion of PANI's emeraldine base to its emeraldine salt form, which was shown to enhance electrical conductivity and pH sensitivity [16]. Depending on the specific application, the solution (~10 mL) was also diluted with 100 mL of deionized (DI) water.

Table 1. Six sets of P3HT:PCBM solutions with different mixing ratios.

	#1	#2	#3	#4	#5	#6
P3HT:PCBM concentration (*w/v*%)	1.00:0.25	1.00:0.50	1.00:0.75	1.00:1.00	1.00:1.25	1.00:1.50

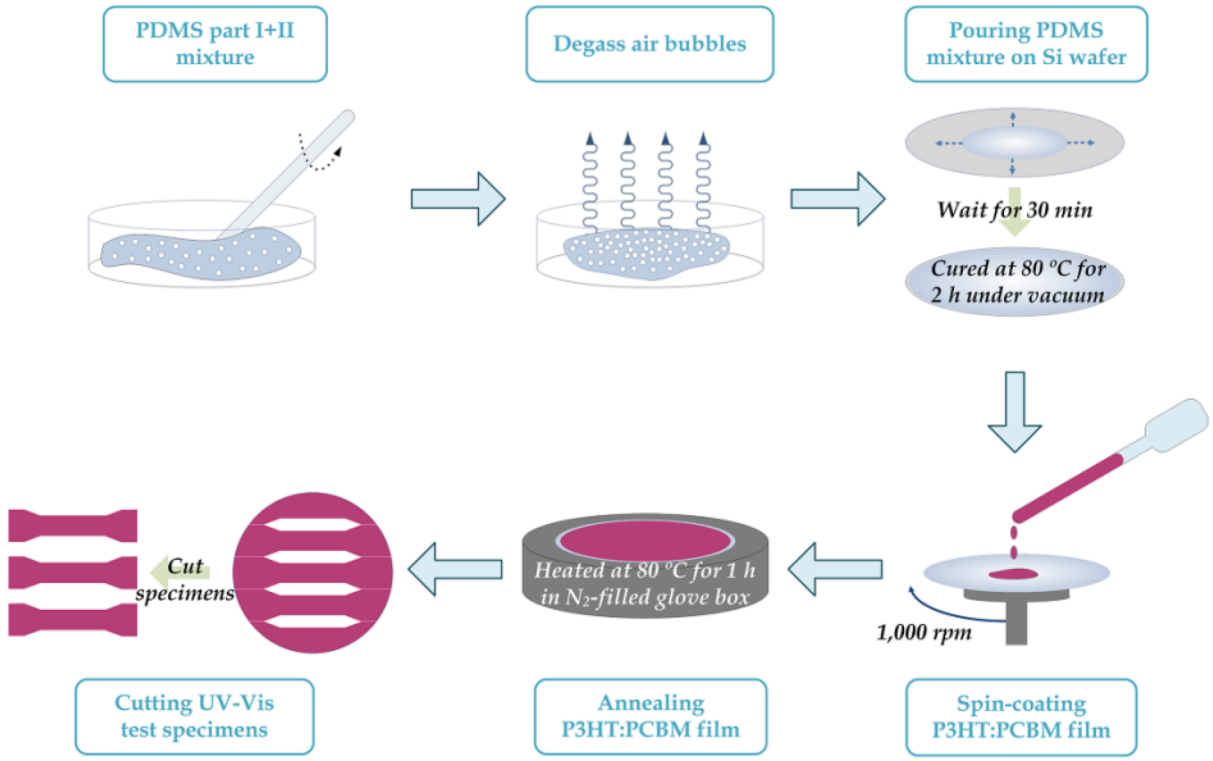

Figure 1. Transparent and flexible PDMS substrates were prepared on 100 mm-diameter silicon wafers and then treated with oxygen plasma. P3HT:PCBM thin films were spin-coated onto PDMS and cut to form dog-bone specimens for UV-Vis characterization.

2.3. UV-Vis Test Specimens

Two different types of UV-Vis test specimens were prepared (using the two solutions described in section 2.2) for depositing P3HT:PCBM and PANI thin films onto transparent substrates. The purpose of preparing these films was to characterize their optical properties (*i.e.*, absorption or transmittance) due to applied strains or different pH buffer solutions. Specimen fabrication is described in this section.

2.3.1. P3HT:PCBM Film Fabrication. Two different transparent substrates, namely PDMS elastomers and glass slides, were used for spin-coating P3HT:PCBM films. For both cases, all six different sets of PP-D solutions (table 1) were used for preparing films characterized by different polymer concentration ratios. First, the PDMS substrates were fabricated using the Dow Corning Sylgard 184 kit, and the process is illustrated in figure 1. The procedure began with measuring 10 g of PDMS base (part I) and 1 g of curing agent (part II). The base and curing agents were mixed together and then manually stirred with a glass rod for 1 min. Although air bubbles were entrapped due to stirring, they were then eliminated during vacuum treatment using a dessicator. Second, the degassed PDMS mixture was poured onto a 100 mm-diameter silicon wafer, which was pre-cleaned using detergent and isopropyl alcohol (IPA). Then, the PDMS mixture, along with the silicon substrate, was cured in a vacuum oven at 80 ºC for 2 h. This

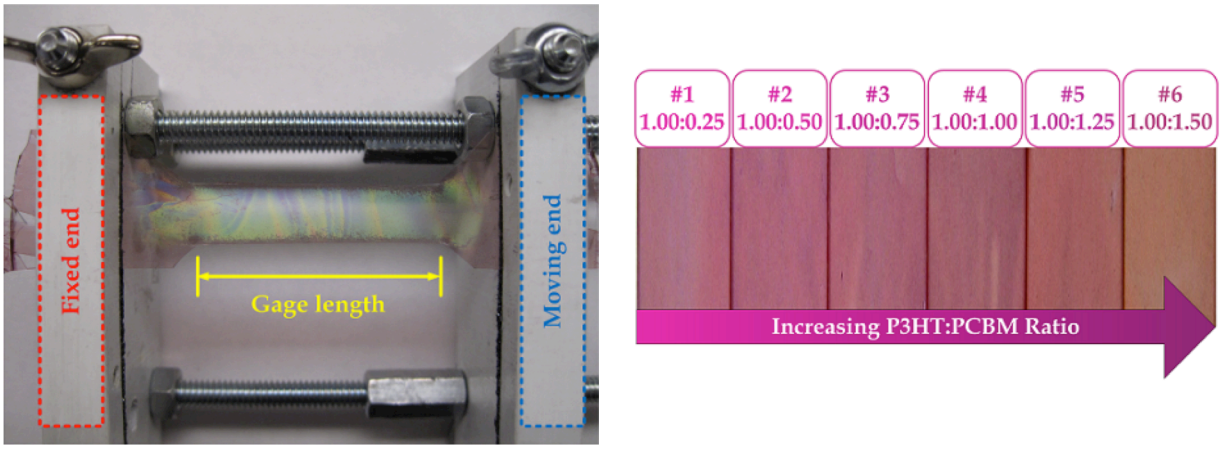

(a) (b)

Figure 2. (a) A P3HT:PCBM dog-bone specimen was mounted in a customized strain apparatus, and the entire setup fit inside the UV-Vis spectrophotometer. The film was deformed by manually adjusting one end of the grip to a certain desired position. (b) Six different sets of P3HT:PCBM thin film that were deposited on glass slides are shown. As P3HT:PCBM ratio increases, the film's color became darker due to higher concentrations of PCBM.

procedure caused the PDMS to crosslink, solidify, and form 1 mm-thick disk-like transparent substrates in which P3HT:PCBM thin films could be deposited. Prior to film deposition, the PDMS substrates were treated with oxygen plasma for 60 s under 150 mTorr at 50 W.

Spin-coating of any of the six PP-D solutions was performed by first spreading at 500 rpm for 5s and then spinning at 1,300 rpm for 60 s, using a Laurell single wafer spin processor (figure 1). The coated films were then annealed on a hot plate at 150 ºC, for 60 min, and in a nitrogen-filled glove box. Finally, the P3HT:PCBM film and PDMS substrate was cut into dog-bone shape specimens with a 38 mm gage length and 12.5 mm width. A completed dog-bone specimen mounted in a customized strain testing apparatus is shown in figure 2a. On the other hand, P3HT:PCBM films were also prepared on cleaned 25×75 mm^2 glass slides (*i.e.*, cleaned using 1:3 hydrogen peroxide-to-sulfuric acid piranha solution). Spin-coating the P3HT:PCBM films followed the same procedure as the PDMS case. Six unique P3HT:PCBM concentration ratio films deposited on glass substrates are shown in figure 2b.

2.3.2. PANI Film Fabrication. PANI-based thin films were deposited onto 25×75 mm^2 glass and PET slides using two different techniques. First, the PANI-DMF solution of section 2.2 was spin-coated onto the glass slide by spreading it at 500 rpm for 5 s and then spinning at 1,000 rpm for 60 s. To attain a more robust and uniform film, spin-coating was repeated five times. In between each coating step, the multilayered film was annealed at 150 ºC for 20 min. The second technique employed was layer-by-layer self-assembly [35]. LbL fabrication requires two oppositely charged solutions. A substrate (*i.e.*, either cleaned glass or PET slides) was sequentially immersed in the two solutions (5 min each) so that oppositely charged self-assembled monolayers could be deposited one after another. For this study, a 1 *w*% PSS solution served as the negatively charged solution, and the diluted PANI solution was its LbL

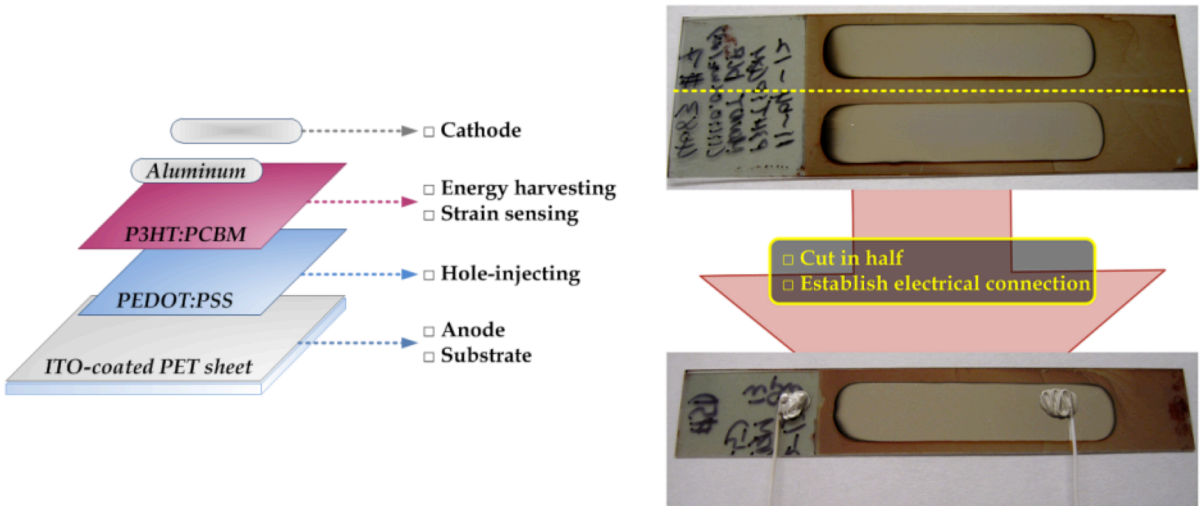

(a) (b)

Figure 3. (a) The design of the P3HT:PCBM-based photoactive device consisted of multiple functional layers. The fabrication process began with depositing the hole-injection layer (PEDOT:PSS) onto an ITO/PET substrate. Then, the P3HT:PCBM layer was spin-coated. A final aluminum electrode layer was deposited on top. (b) The completed film was cut in half to create two identical test specimens and was used as is for the entire study.

counterpart. PSS was dissolved in DI water by 30 min of bath ultrasonication (135 W and 42 KHz). For the positively charged solution, diluted PANI was used, because its aqueous nature was compatible with LbL and facilitated the deposition of the protonated polyaniline. After depositing each monolayer, the slide was rinsed with DI water for 3 min to remove loosely bound materials and then followed by 10 min of drying using compressed air. A total of 50 and 20 bilayers of PANI/PSS films were deposited onto the glass and PET slides, respectively.

2.4. Flexible Photoactive Sensors

The photoactive thin films that were designed for photocurrent generation and sensing validation tests were fabricated using the procedure illustrated in figure 3a. First, ITO/PET slides (25×75 mm^2) were cleaned by immersing them in separate solutions of diluted detergent, DI, and then IPA (for 10 min each) while subjected to bath ultrasonication. Then, the slides were dried using compressed air. Second, the ITO layer's surface energy was reduced by subjecting it to argon (Ar) plasma at 50 W and 150 mTorr for 60 s. It should be noted that Ar plasma was used instead of oxygen plasma for minimizing possible damage to the ITO layer (*i.e.*, due to the inert nature of Ar). Next, the hole-injection layer was deposited onto the Ar plasma-treated ITO by spreading the PEDOT:PSS solution at 500 rpm for 5 s and spinning at 2,500 rpm for 60 s. The entire slide was then annealed for 30 min and on a hot plate operating at 80 ºC in a nitrogen-filled glove box. This procedure completed the preparation and fabrication of one of the electrodes.

The next step entailed spin-coating the P3HT:PCBM BHJ layer, which was responsible for converting photonic energy to electrical energy and for sensing, as will be described later. Here, only the #5 P3HT:PCBM solution was used (table 1). The solution was pipetted onto the ITO/PET and PEDOT:PSS surface, spread at 500 rpm for 5 s, and then spun at 1,300 rpm for 60 s to form a uniform thin film. This was followed by annealing on a hot plate at 80 ºC for 60 min in a nitrogen-filled glove box. It should be noted that the P3HT:PCBM layer was covered with a petri dish to slow the rate of drying and solvent evaporation, since it was already demonstrated that slow drying could minimize PCBM phase separation [36, 37]. Then, two aluminum electrodes (8.9×38 mm^2) were deposited onto the annealed P3HT:PCBM BHJ using a Lesker DC sputterer operated at 450 W for 10 min. The completed film was cut in half to obtain two identical test specimens, and each specimen's dimension was 1.25×7.5 mm^2 as shown in figure 3b. To facilitate photocurrent measurements, additional single-strand wires were connected to the ITO and Al electrodes using conductive silver epoxy.

3. UV-Vis Characterization

The optical properties of the P3HT:PCBM BHJ and PANI-based films (using specimens from section 2.3) were characterized using an Evolution-220 UV-Vis spectrophotometer. First, the light absorption response of the six different sets of P3HT:PCBM films was obtained. The purpose was to study whether the relative concentrations of PCBM influenced the BHJ's light absorption properties. Second, the absorption spectra of strained P3HT:PCBM films were also measured and characterized. Lastly, the optical transmission spectra of PANI-based films treated with different pH buffer solutions were investigated for understanding their pH sensitivity.

3.1. P3HT:PCBM Light Absorption: Unstrained

Using P3HT:PCBM films spin-coated onto glass slides (section 2.3.1), the UV-Vis absorption properties of the six different set of films (table 1) were characterized. In particular, the objective was to investigate whether or not the relative concentration of PCBM affected the film's optical response. In fact, it was found that P3HT molecules formed lamellar crystallite structures after thermal annealing and solvent evaporation of the BHJ layer [38]. Multiple layers of this lamellar structures were stacked as shown by results obtained using X-ray diffraction [39]. In this study, it was hypothesized that P3HT's molecular arrangement was affected by the existence and concentration of PCBM molecules. If so, then the P3HT:PCBM BHJ's UV-Vis light absorption spectra would consist of unique features specific to the concentration of PCBM used.

Six representative light absorption spectra corresponding to the six different P3HT:PCBM mixing ratios were obtained and is plotted in figure 4a. It should be mentioned that each absorption spectrum was normalized by its peak light absorption (at ~500 nm wavelength). From figure 4a, it is clear that all the six absorption spectra are characterized by two major peaks at ~335 nm and ~510 nm, as well as two minor peaks at ~550 nm and ~600 nm. The peak at ~335 nm indicates light absorbed by PCBM molecules [32]. The magnitude of relative absorption at the ~335 nm peak varies with PCBM concentration, but the peak wavelength remains consistent. The other major peak (~510 nm) and two minor peaks (~550 and ~600

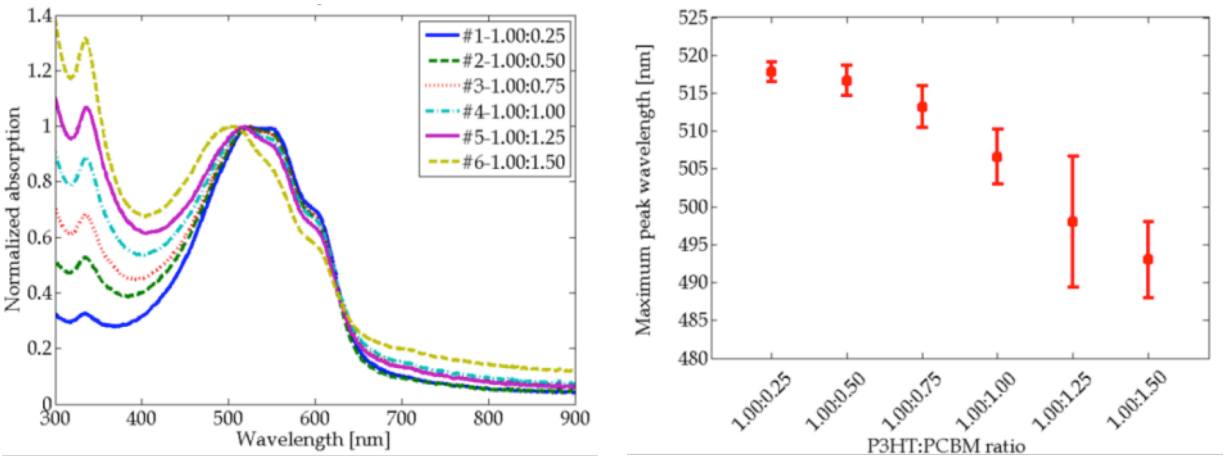

(a) (b)

Figure 4. (a) The normalized UV-Vis absorption spectra of six different sets of P3HT:PCBM thin films (each with a unique mixing ratio) are plotted. Normalization was performed with respect to the light absorption measured at the main peak of ~500 nm. Strain affected peak absorption and the two shoulders at ~550 and ~600 nm. (b) The main absorption peak is plotted as a function of P3HT:PCBM maxing ratio. The maximum peak wavelength decreased (or blue-shift) as P3HT:PCBM ratio increased.

nm) correspond to light absorbed by P3HT molecules [32]. The main peak at ~510 nm occurs due to light absorption relevant to intramolecular π-electron excitation, while the other two shoulders are attributed to intermolecular electron excitations [32].

Interestingly, the main ~510 nm peak shifts from a longer to that of a shorter wavelength (*i.e.*, blue-shifts) as PCBM content increases. The wavelengths of these main peaks are plotted in figure 4b with respect to the film's PCBM concentrations (*i.e.*, different P3HT:PCBM ratio). It should be noted that higher energy would be needed for generating excitons (*i.e.*, excited hole and electron pairs) as the maximum peak wavelength becomes shorter. This is because light characterized by a shorter wavelength possesses greater energy. On the other hand, the two shoulders become increasingly suppressed as PCBM concentration increases. This result means that, the presence of excessive PCBM molecules with respect to P3HT causes the BHJ or thin film to become less effective at promoting intermolecular π-electron excitations. However, PCBM is indispensable as part of the BHJ structure, since it serves as the electron acceptor; so, the significance of this result is that an appropriate concentration of PCBM molecules is required for guaranteeing effective electron-hole separations [40]. As a result, mainstream efforts have focused on using P3HT:PCBM mixing ratios ranging from 1.00:1.00 to 1.00:1.25 (*e.g.*, for organic photovoltaic applications), as opposed to say a 1.00:0.25 ratio. In this study, a 1.00:1.25 (*i.e.*, the #5 sample set as listed in table 1) is selected, since preliminary results suggest optimal photocurrent generation and high strain sensitivity [40].

3.2. P3HT:PCBM Light Absorption: Strained

Variations in light absorption of P3HT:PCBM films in response to applied strains had been investigated by a preliminary study conducted by Ryu and Loh [29]. It was found that light absorption, or the number of photons absorbed by P3HT, increased with the application of higher tensile strains. Since absorbed photons contributed to exciton formation and photocurrent generation, the result was the increase in the magnitude of photocurrent as higher levels of strain were applied. Despite confirming photocurrent-based strain sensing, this previous study did not reveal how the P3HT molecules became more efficient photon absorbers under larger mechanical deformations. To address this question, UV-Vis was employed for characterizing how the six different sets of P3HT:PCBM thin films' absorption spectra (table 1) changed with applied tensile strains, as well as the effects of relative PCBM concentration.

Here, P3HT:PCBM thin films spin-coated onto flexible and transparent PDMS substrates were mounted in a customized load frame, and a one-cycle tensile load pattern was executed to strain each specimen (figure 2a). The entire test setup, including the load frame and film, were fit inside the measurement chamber of an Evolution-220 UV-Vis spectrophotometer. Then, each film was strained to ~12% and in ~3% increments. At each load step (including the 0% cases before and after loading), the spectrophotometer was commanded to obtain the light absorption spectrum. Thus, a total of nine UV-Vis absorption spectra were obtained for each test.

Figure 5a plots a set of five UV-Vis absorption spectra acquired from the load testing of a P3HT:PCBM film; the absorption spectra for the unloading steps are not shown for clarity. As applied tensile strain increases, the film's absorption spectrum (*i.e.*, across the entire bandwidth of wavelengths tested, which is 300 to 900 nm) shifts upward and increases. The results of figure 5a are not due to Poisson's effect but rather due to molecular and organizational changes of the P3HT:PCBM BHJ. Poisson's effect would instead decrease absorption due to thinning of the film during applied tensile strains. It should also be noted that light absorbed by P3HT, which is primarily due to the major peak at ~500 nm and between the two shoulders from 400 to 650 nm, contributes to generating photocurrent (section 3.1). Light absorption near 335 nm is, again, due to PCBM.

On the other hand, absorption measured at other wavelengths is not the true absorption of the film, but rather, it is an artifact of the UV-Vis measurement system. This can be explained by considering how the absorption spectrum is determined by a spectrophotometer. In particular, light absorption is not directly measured but is calculated using the Beer-Lambert law by considering the light transmitted through a sample and the incident light.

$$A = -\log_{10}\left(\frac{I}{I_0}\right) \tag{1}$$

where A is absorption, and I and I_0 are the intensities of transmitted and incident light, respectively. However, if light is scattered or reflected, then I decreases dramatically to cause the system to report a large absorption value. Therefore, a more accurate analysis can be conducted only if light absorbed by P3HT and in the 400 to 650 nm range is considered as the primary source of photonic energy for photocurrent generation.

For each film tested and for each of the nine absorption spectra recorded, a peak-picking algorithm has been implemented to identify the magnitude of peak light absorption and its corresponding light wavelength. Eq. 2 is then utilized for calculating normalized peak absorption (PA_{norm}), by dividing the peak absorption corresponding to a certain level of strain (PA) by the peak absorption for the 0% strain case ($PA_{0\%}$).

$$PA_{norm} = \frac{PA}{PA_{0\%}} \tag{2}$$

Figure 5b shows a representative result that plots normalized light absorption versus applied strain (*i.e.*, obtained from one P3HT:PCBM film and one particular test). A linear least-squares regression line is also fitted to the raw data, and strong linear correlation is observed. The slope of the regression line can be regarded as the optical strain sensitivity of the P3HT:PCBM thin films. On the other hand, figure 5c tracks the peak wavelength shifts at different levels of applied strain. These results support the hypothesized that strain affects the effective conjugation length of P3HT [32]. It has already been shown that P3HT with longer conjugation lengths are characterized by maximum light absorption at longer light wavelengths [32]. Thus, from figure 5c, one can conclude that P3HT molecules are influenced by applied strains and responds by changing its effective conjugation length. During low levels of applied strains (*i.e.*, < 2%), it is observed that the change in P3HT conjugation length is not significant. For the strain sensing validation tests conducted in this study, films have only been strained to 0.5% tensile strain. This means that, at these low levels of applied strain, strain-sensitive photocurrent was not due to strain-induced conjugation length changes of P3HT molecules.

On the other hand, when considering all six sample sets, figure 5d shows that optical strain sensitivities tend to increase as the P3HT:PCBM ratio increases. This trend can be explained in terms of strain-induced crystallinity changes of P3HT molecules within the BHJ structure. As mentioned in section 3.1, P3HT molecular crystallinity is determined mostly by the relative concentration of PCBM within the BHJ structure, and P3HT tends to present itself in a less crystallized form when there are more PCBM molecules. Thus, it is expected that P3HT with a lower degree of crystallinity (*i.e.*, films with more PCBM) is more susceptible to strain, which results in higher strain sensitivities. This explanation is consistent with the results obtained and shown in figures 5a and 5d.

3.3. Optical Properties of PANI-based Thin Films for pH Sensing

According to section 2.3.2, two different types of PANI-based thin films (*i.e.*, spin-coated and LbL) were deposited onto glass slides and tested to characterize how their optical properties change after immersing them in different pH buffer solutions. In general, pH 1 buffer solution was pipetted onto the as-fabricated PANI-based films, and the solution was exposed to the film for 10 s. All the films were treated with the pH 1 buffer solution first for facilitating wetting of the hydrophobic PANI-based film. Exposing the film to a strong acid (*i.e.*, pH 1 buffer solution) helped decrease the film's surface energy. Then, excess solution was removed, and the film was dried using a heat gun operating at 90 ºC. The same procedure was repeated such that the films were exposed to different pH buffer solutions (from pH 1 to 13).

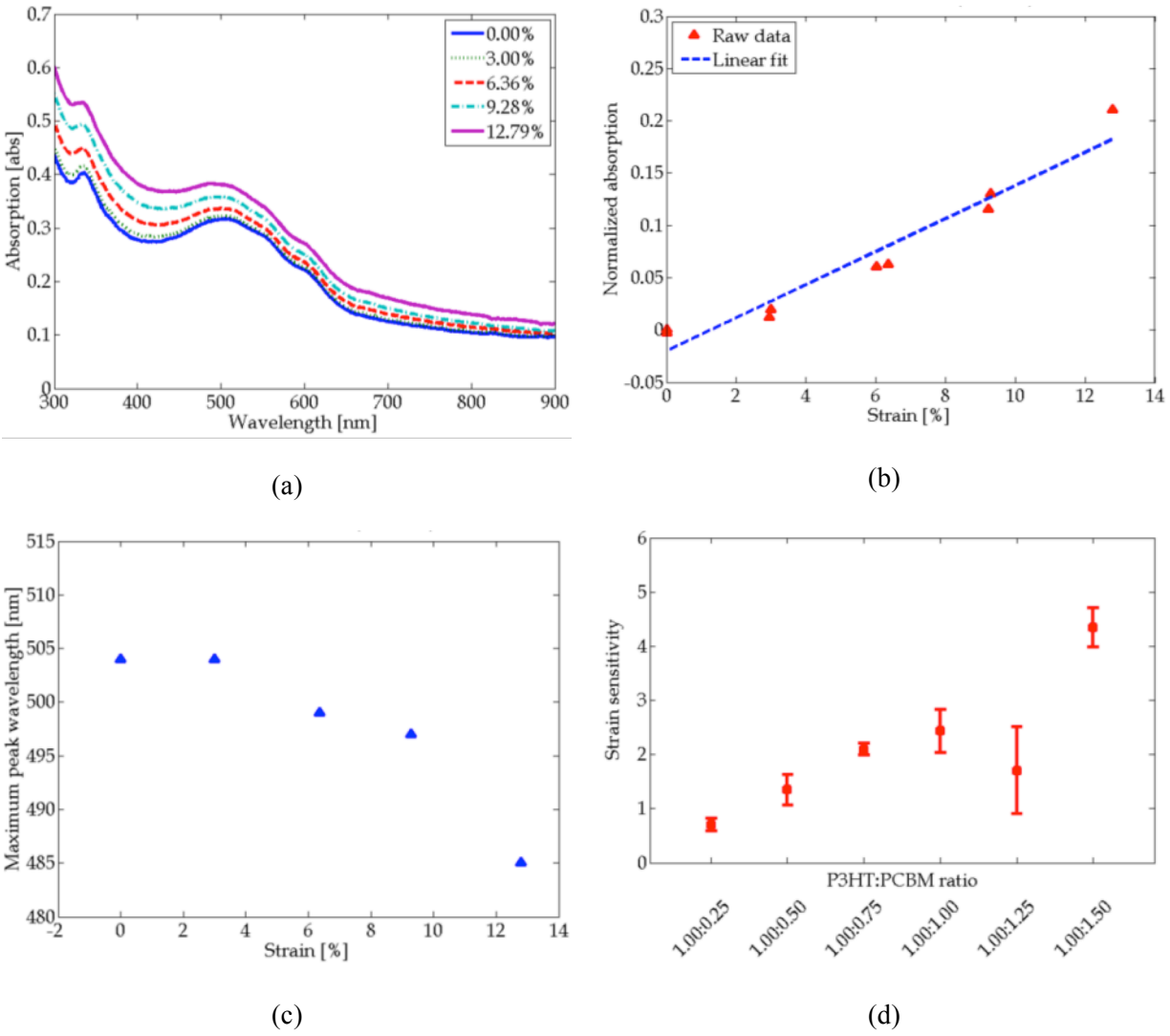

Figure 5. P3HT:PCBM thin film's light absorption responses were obtained at various tensile strains levels. (a) Five light absorption spectra obtained during the tensile loading cycle are shown. Light absorption increased with the application of greater tensile strains. (b) The peak absorption (at ~500 nm) corresponding to different levels of applied strain were extracted and plotted. A linear least-squares line was fitted for calculating strain sensitivity. (c) The maximum peak wavelength was found to decrease as strain was increased. This meant that P3HT absorbed shorter wavelengths of light (or higher energy) at higher strains. (d) The strain sensitivities are plotted with respect to P3HT:PCBM ratio, and the results show an increasing trend as P3HT:PCBM ratio increases.

Figure 6a shows a picture with seven representative spin-coated PANI films treated with acidic buffer solutions (*i.e.*, pH 1 to 7). The other six PANI films treated with alkaline buffer solutions (*i.e.*, pH 8 to 13) are not shown, because the color change was not as significant. Regardless, from figure 6a, it can be seen that color change in the acidic range is dramatic and transitions from green to purple as pH increases. In addition to the films' colorimetric response, the light transmittance spectra have also been obtained. Transmittance has been measured using the Evolution-220 UV-Vis spectrophotometer.

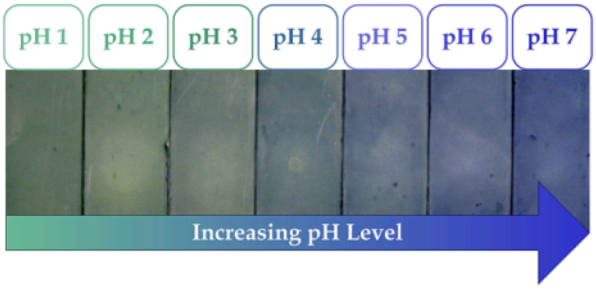

(a)

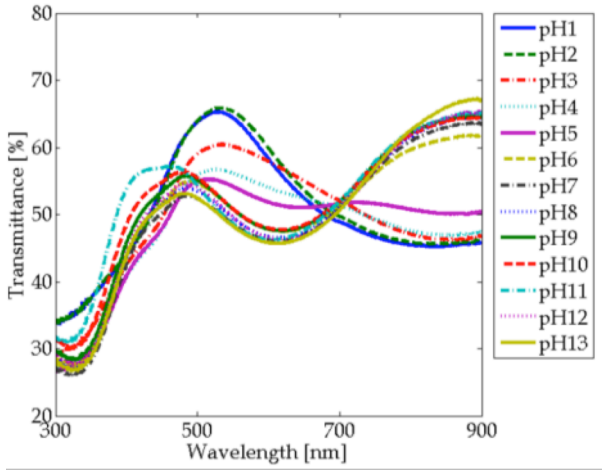

(b)

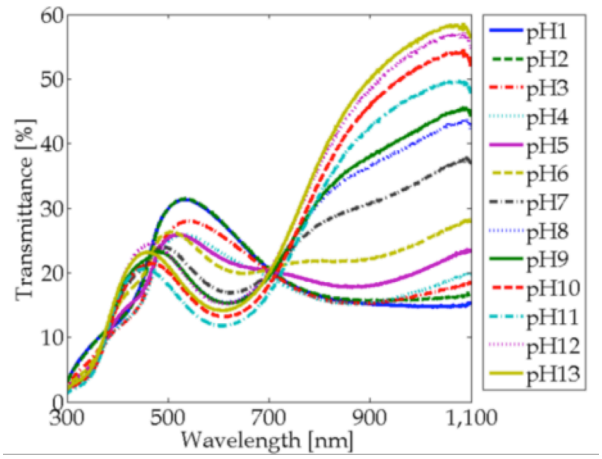

(c)

Figure 6. Two sets of PANI-based thin films were tested and treated with pH 1 to 13 buffer solutions. (a) The picture shows that the color of the spin-coated PANI film transitioned from green to purple as pH increased from 1 to 7. (b) The spin-coated and (c) LbL PANI film's light tranmisttance spectra depended on pH. The LbL PANI films exhibited linear and more dramatic changes in transmittance as pH was increased.

Figure 6b shows an overlay of the light transmittance spectra of a spin-coated PANI film treated with pH 1 to 13 buffers. The most significant change of transmittance due to pH occurs in two separate ranges of light wavelengths, namely 500 to 600 nm and 800 to 900 nm. When the film is exposed to a pH 1 buffer, the transmittance peak is ~500 nm, which corresponds to green light. The transmittance peak decreases as the buffer solution's pH increases and finally disappears above pH 4. Instead, the maximum peak shifts to ~450 nm when the films have been treated with greater than pH 4 buffers, which is in the blue/purple light wavelength range. These light transmittance peaks correspond to the observed colorimetric response of the PANI films as shown in figure 6a.

As mentioned earlier in this section, the LbL PANI-based films have also been subjected to pH testing, and a representative result that overlaid 13 UV-Vis transmittance spectra is shown in figure 6c. One can compare the result presented in figure 6c with the ones obtained using the spin-coated PANI film shown in figure 6b and find that the sensitivity to pH is significantly different. First, in light wavelengths

between 500 and 600 nm, the LbL films' transmittance decreases in a more linear fashion as pH is increased from pH 1 to 13 (figure 6c), as compared to that of figure 6b where light transmittance is more sensitive to pH 3 to 6 buffer solutions. Even more interesting is the LbL film's transmittance properties above 800 nm, where it exhibits dramatic sensitivity to pH changes. In addition, the transmittance spectrum corresponding to each pH case is well separated and ideal for sensing. The change in transmittance is approximately four-fold, increasing from ~15% for pH 1 to ~60% for pH 13. As a side note, the LbL PANI-based film exhibits much better durability and has been able to stay intact after repeated cycles of pH 1 to 13 testing. Based on these results, the LbL film is selected for pH sensing and for the remainder of this study.

4. Photocurrent-based Multi-modal Sensing

The underlying premise for achieving multi-modal sensing was to interrogate P3HT:PCBM thin films (*i.e.*, deposited on ITO/PET following the procedures outlined in section 2.4) using different bandwidths of light and then measuring the corresponding generated DC photocurrent. First, the results from section 3 were analyzed for determining two light wavelength ranges for the selective sensing of strain and pH. Selectivity and stimuli sensitivity were two major concerns for achieving optimal multi-modal sensing performance. Second, the films were validated for photocurrent generation due to the illumination of broadband and narrowband light. Lastly, sensing of strain and pH using one multi-layered thin film was demonstrated through laboratory experiments.

4.1 Selection of Light Wavelengths for Strain and pH Sensing

The UV-Vis measurements presented in sections 3.2 and 3.3 have been used for defining appropriate light wavelengths for multi-modal strain and pH sensing. First, the 400 to 650 nm range is most ideal for strain sensing, since this is the active range of wavelengths in which light is absorbed by P3HTs and that absorption is also sensitive to strain (see figure 5a). As shown in figure 5a, since absorption increases as strain is increased, a larger photocurrent is expected to be generated too. On the other hand, section 3.3 and figure 6c show that there are two regions in which the LbL PANI film's light transmittance is extremely sensitive to pH, namely 500 to 600 nm and greater than 800 nm. However, maximum sensitivity is achieved in the near-infrared (IR) range (*i.e.*, >800 nm).

In addition to identifying the regions of the light absorption/transmittance spectra in which the P3HT:PCBM-based films are most sensitive to strain or pH, it is just as important to find the appropriate wavelength range in which strain sensing is maximized but pH sensing is suppressed (and vice versa). Multi-modal sensing requires that one be able to differentiate and attribute one response measurement to the external stimulus (in this case, strain/deformation or pH/corrosion). Thus, based on the results shown in figures 5 and 6, two different optical filters were chosen for interrogating the photoactive film: 450±40 nm band-pass (BP) filter for strain sensing and >800 nm dichroic long-pass (LP) filter for pH sensing. Both filters were purchased from Edmund Optics and can be fitted onto the 150 W Oriel solar simulator light source. Figure 7 shows the light transmittance spectra of the BP and LP filters.

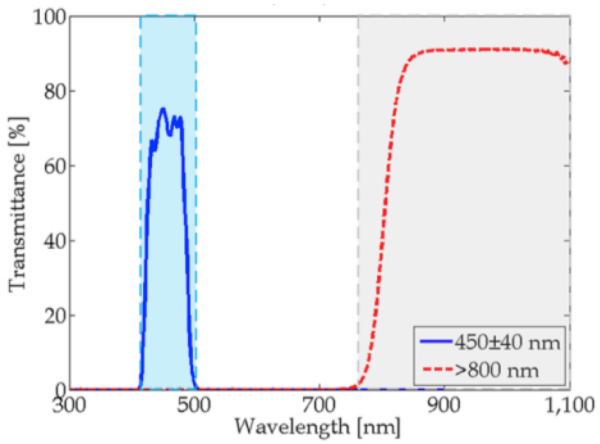

Figure 7. Two optical filters, namely 450±40 nm band-pass and >800 nm long-pass filters, were selected and fitted on the Oriel solar simulator for wavelength-based multi-modal sensing. Blue light was designated for strain and near-IR light for pH.

4.2 Experimental Setup

The P3HT:PCBM-based thin films fabricated using the procedure outlined in section 2.4 were used as is, and a picture of the general experimental setup is shown in figure 8. Each P3HT:PCBM-ITO/PET specimen was mounted onto a Test Resources 150R electromechanical load frame. First, the load frame was commanded to preload each film to 5.0 N so as to flatten the specimen. For strain tests, the load frame could then execute different pre-defined load patterns (*e.g.*, tensile cyclic patterns). Second, an Agilent 34401A digital multimeter (DMM) was connected to the film's two electrodes and was configured to measure DC current using a sampling rate of 2 Hz. On the other hand, the films' excitation and light source was light generated by a 150 W xenon lamp housed in an Oriel solar simulator equipped with an air mass 1.5 global (AM 1.5G) broadband optical filter. Depending on the specific test conducted, the aforementioned 450±40 nm BP filter or the >800 nm LP IR filter could be fitted onto the solar simulator for shining narrowband light onto the film specimens. The picture of figure 8 shows the illumination of blue light after fitting the solar simulator with the AM 1.5G and BP filters. In the following sections, photocurrent generation and multi-modal sensing of the photoactive thin films were validated using this test setup.

4.3 Photocurrent Generation

One of the first tests conducted was to verify the generation of DC photocurrent when the P3HT:PCBM-ITO/PET films were illuminated by three different bandwidths of light: AM 1.5G broadband, blue light using the 450±40 nm BP filter, and near-IR light using the >800 nm LP filter. The experimental setup described in section 4.2 and figure 8 was utilized. For each test case, light was turned on for ~120 s and then off for ~30 s, and this was repeated three times. It should be mentioned that each film was fixed by mounting them in the load frame, but the films were not strained.

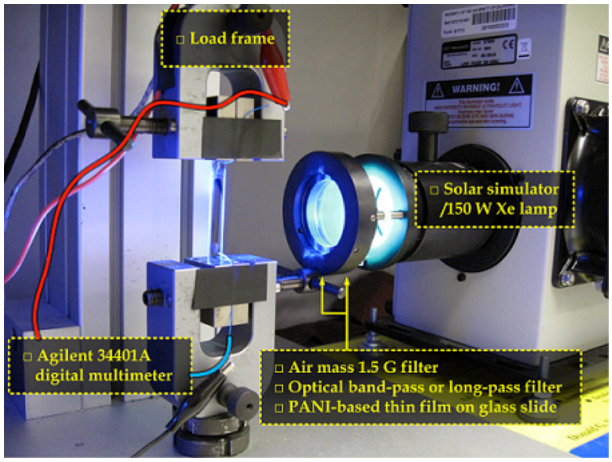

Figure 8. The photocurrent-based multi-modal sensing test setup is shown. The picture shows one test in which blue light was illuminated on the P3HT:PCBM specimen that was mounted in the Test Resources load frame. The resulting generated photocurrent was measured using an Agilent DMM.

Figure 9a plots the overlay of three representative photocurrent time histories obtained after testing the same #5 P3HT:PCBM-based specimen. The three photocurrent generation results correspond to the three different bandwidths of light that was used to illuminate the specimen. In general, all three cases verified generation of DC photocurrent when the light source was turned on (*i.e.*, regardless of the filter used). Although the film does not appear to generate photocurrent when near-IR light is used, closer examination of the results show that the magnitude of photocurrent was in the μA range. This occurs because photons in the near-IR wavelengths do not have sufficient energy for eliciting the P3HT:PCBM BHJ's photovoltaic response. The P3HT molecule's π-electrons at the highest-occupied molecular orbit cannot overcome the energy gap (~2.2 eV) to become excited to a higher energy level or lowest unoccupied molecular orbit [32].

In contrast, the magnitudes of generated photocurrent for the broadband and blue BP cases are ~1 and ~0.25 mA, respectively (figure 9a). As it can be observed from figure 9a, the film's broadband photocurrent response decays with time. It is assumed that P3HT was degraded by UV light, thereby reducing photocurrent generation [41]. For the case when the film was illuminated by blue light (410 to 490 nm), photocurrent generation remains stable throughout multiple cycles of light on/off testing. The overall decrease of photocurrent magnitude can be attributed to fewer photons available for excitation and photocurrent generation, simply because of the use of the BP filter.

Besides photocurrent time histories, current-voltage (*IV*) responses have also been obtained using an Agilent B2901A Source Measure unit. Figure 9b plots the *IV* responses of one film being illuminated by the three aforementioned light sources, as well as when all light is turned off. The results presented in figure 9b are consistent with those found in figure 9a. The short-circuit currents (I_{SC}) obtained from the *IV* responses are comparable to the magnitudes of DC photocurrent time histories recorded. The lower values of photocurrent shown in figure 9a, as compared to I_{SC} in figure 9b, is due to the fact these P3HT:PCBM-based thin films have been tested in ambient environment (*i.e.*, oxygen- and moisture-rich), which has been shown to cause degradation. As for the open-circuit voltage (V_{OC}), only non-zero values have been obtained for the broadband and blue light cases (*i.e.*, 0.4 and 0.3 V, respectively). The presence of a built-

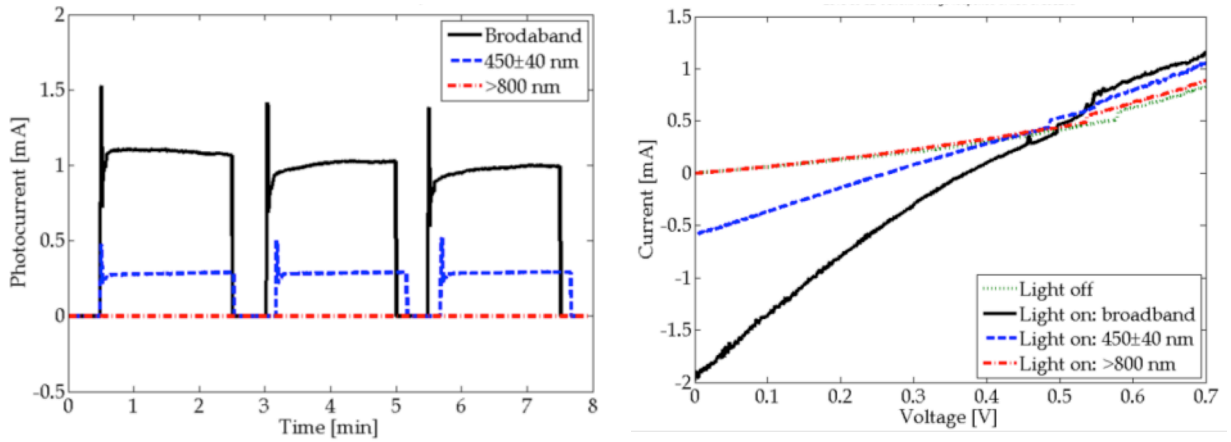

(a) (b)

Figure 9. Photocurrent generation of a #5 P3HT:PCBM sample set was characterized with three different light sources: broadband, blue, and near-IR light. (a) The photocurrent time histories were obtained and overlaid. Three cycles of ~120 s of light on and ~30 s of light off were conducted. (b) Current-voltage responses were obtained in the dark and when illuminated by the three different light sources.

in voltage allows hole-electron pairs to separate and generate photocurrent. Similarly, this result also confirms that near-IR light does not induce photovoltaic response of the film, and photocurrent generation is due to the photoelectric effect, which is not expected to be sensitive to strain.

4.4. Strain Sensing

Using the test setup shown in figure 8, strain sensing validation tests were conducted on P3HT:PCBM-ITO/PET specimens after they have been characterized for their photocurrent generation and *IV* properties. After mounting the specimen in the Test Resources load frame and then pre-loading, the load frame was commanded to execute a three-tensile cyclic strain pattern to 5,000 με (0.5%) and using a 10,000 με-min^{-1} (1% min^{-1}) load rate. Meanwhile, the Oriel solar simulator equipped with a blue (450±40 nm) band-pass filter illuminated the film, and DC photocurrent was measured using an Agilent DMM. The load frame's crosshead displacement and load were recorded at 30 Hz, and photocurrent was sampled at 2 Hz. All the data were time-stamped and recorded using *LabVIEW*. The aforementioned tensile cyclic test was also repeated using the near-IR light source.

As hypothesized in section 3.4 and shown in figure 10a, the photocurrent generated by shining 450±40 nm or blue light on the P3HT:PCBM-based film is sensitive to strain. In contrast but as expected, near-IR light did not generate photocurrent that varied due to applied strains (figure 10b). In figure 10a, it can be seen that the normalized change in DC photocurrent (I_N) increases in tandem with increasingly applied tensile strains, and it also decreases in the same linear fashion during unloading. Photocurrent at time (t) or I_t, is normalized with respect to its baseline photocurrent immediately before the initiation of strain testing (I_0). which is calculated using Eq. 3.

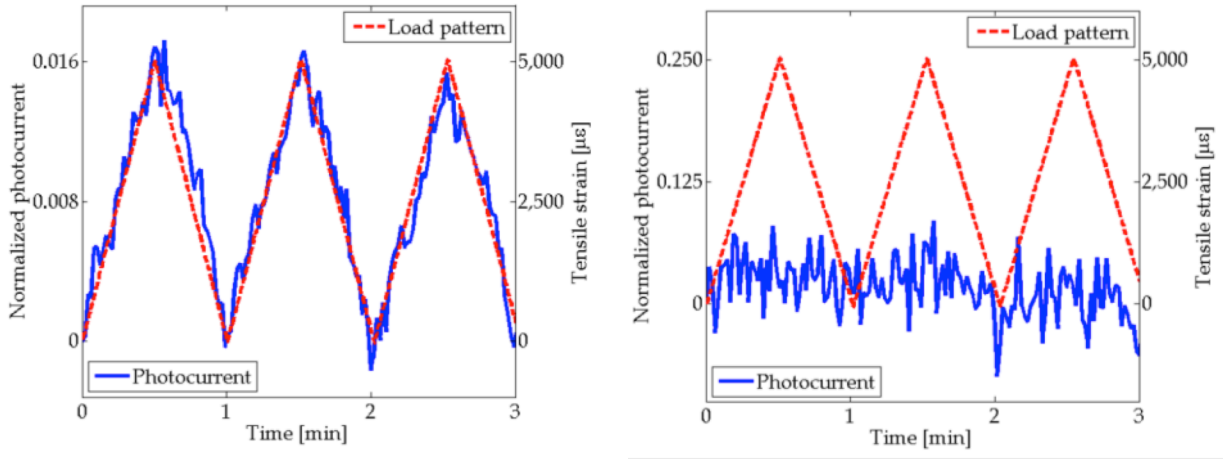

Figure 10. The strain sensing response of a P3HT:PCBM-ITO/PET test specimen was validated. (a) When the specimen was illuminated by blue light, the generated photocurrent shows excellent agreement with the applied strain pattern. The average strain sensitivity was calculated to be ~3.2. (b) In contrast, photocurrent generated due to near-IR light illumination was not sensitive to strain.

$$I_N = \left(I_t - I_0\right)/I_0 \tag{3}$$

In figure 10a, the normalized photocurrent also shows a high degree of agreement with the triangular (or saw-tooth) load pattern. It should be noted that the normalized photocurrent was further processed to yield the down-sampled dataset of normalized photocurrent, $I_{N,ds}$. Down-sampling was accomplished by calculating the average of three consecutive $I_{N,i}$ and using Eq. 4.

$$I_{N,ds} = \left(I_{N,i} + I_{N,i+1} + I_{N,i+2}\right)/3 \tag{4}$$

Strain sensitivity (S_S) or gage factor can be calculated for each loading and unloading step using Eq. 5.

$$S_s = I_N/\varepsilon \tag{5}$$

where ε is applied strain. The average strain sensitivity is approximately 3.2, which is also consistent with results obtained in a previous study [28]. This result attests to the fact that the 410 to 490 nm range is suitable for strain sensing.

4.5. Load Rate Effects on Strain Sensing

In addition to the tests conducted in section 4.4, the effects of load rate on the film's strain sensing response were also investigated. The Test Resources 150R load frame was commanded to strain the films using the same three-cycle load pattern, but the load rate was varied from 0.5% to 20% min^{-1}. The other experimental details were kept the same; specifically, blue light was used for interrogating the film.

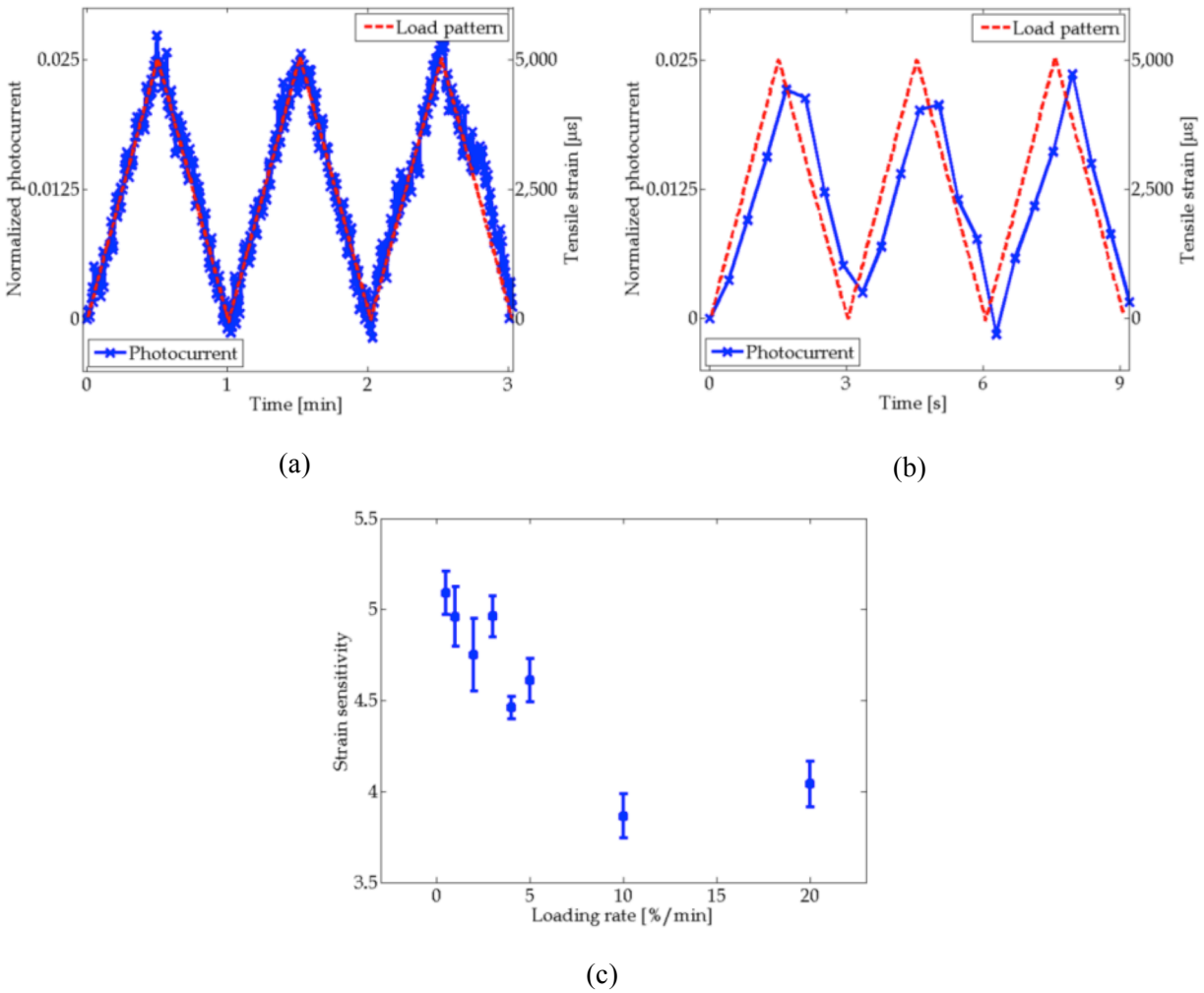

Figure 11. Strain sensing tests were conducted, and the photocurrent time histories for films illuminated by blue light and tested using loading rates of (a) 1% min^{-1} and (b) 20% min^{-1} are plotted. (c) It was found that strain sensitivity decreased as the loading rate increased.

Figures 11a and 11b show two representative strain sensing results obtained from testing using load rates of 1% and 20% min^{-1}. In the case of the slower load rate (figure 11a), the DC photocurrent time history exhibits excellent agreement with the applied tensile cyclic strain pattern; phase lag, if any, is negligible. However, load rates greater than 5% min^{-1} have resulted in the film's photocurrent time history response to lag behind the applied load (figure 11b). In addition to considering phase lag, the film's strain sensitivity is also calculated for each load rate test result. It has been found that the film's average strain sensitivity decreases with increasing load rate, although it seems to plateau beyond 10% min^{-1} (figure 11c). More data is required at these higher load rates for accurately characterizing any possible plateauing effects, which is the subject of future investigations.

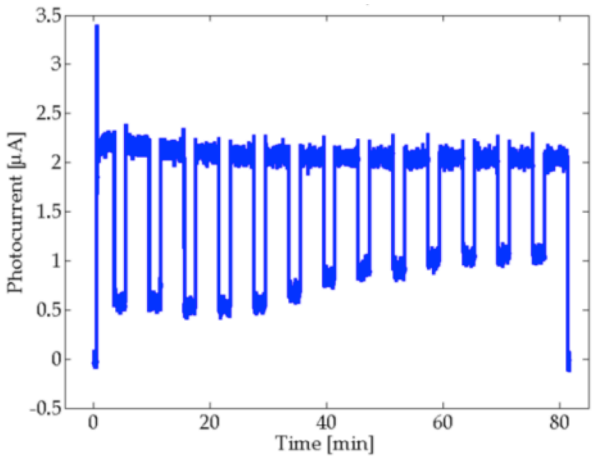

Figure 12. The validation of pH sensing was conducted using near-IR light. The photocurrent generation time history of a pH sensing test is presented. During testing, the PANI-based film (after being immersed in a pH buffer solution) was placed in the light path for 2 min and then removed for 4 min. The procedure was repeated for all of the 13 different pH buffer solutions.

4.6 pH Sensing

Validation of pH sensing was accomplished by integrating the LbL PANI-based thin film (section 2.3.2) with the #5 P3HT:PCBM-ITO/PET specimen. Similar to section 4.5, the experimental setup shown in figure 8 was employed. For this test, the PANI-based film, which was deposited onto a glass slide, was placed on top of a P3HT:PCBM-based film. The PANI-based film was not deposited onto the photoactive film so that the P3HT:PCBM film could be used for other tests. The PANI-based film was also placed in between the light source and P3HT:PCBM film so that changes in light transmittance of the PANI-film (*i.e.*, due to pH) would affect the spectrum of light transmitted. Then, pH sensing tests were conducted by immersing the LbL PANI-based film in different pH buffer solutions (similar to section 3.3).

Photocurrent-based pH sensing tests were conducted by shining blue or near-IR light onto the PANI- and P3HT:PCBM thin films for the entire duration of the test. For each pH case, the PANI-based film was removed and immersed in the corresponding buffer solution for 4 min. During this time, photocurrent was still recorded even without the presence of the PANI-based film. Then, the treated film was placed back in the light path for 2 min. After this cycle, the PANI-based film was treated with the next increment of pH buffer solution, and the entire procedure was repeated for all 13 pH levels. DC photocurrent was measured using an Agilent DMM and throughout the entire test of ~80 min, and a representative result is shown in figure 12. This pH sensing test was also repeated twice so that the films could be interrogated once using blue light and the next time using near-IR light.

Figure 12 shows a film's photocurrent time history response when it is illuminated by near-IR light (>800 nm) and the PANI-based film has been treated with pH 1 to 13 buffer solutions. One can see from figure 12 that, while the baseline photocurrent remains stable at ~2 μA, the magnitude of photocurrent depends on what pH buffer solution the film has been subjected to. Instead of considering the absolute magnitude of photocurrent, one can calculate the percent change of photocurrent with respect to the pH 1 case:

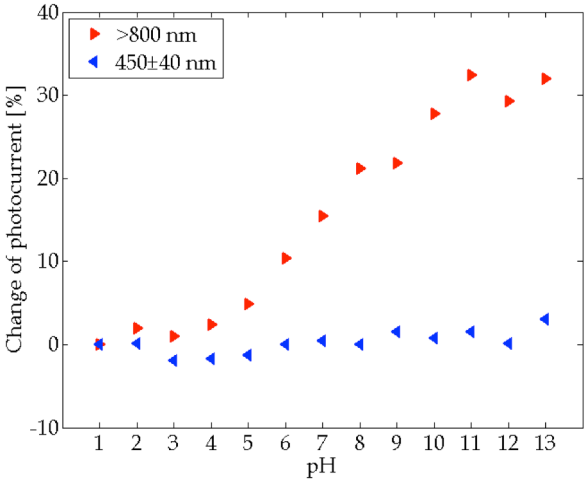

Figure 13. The validation of pH sensing was conducted using blue and near-IR light. The change in photocurrent was calculated and plotted as a function of pH. The result confirmed that near-IR light activated the pH sensing mode, and blue light did not generate pH-sensitive photocurrent.

$$\%\Delta I_{pH} = \left(I_{ave,pHn} - I_{ave,pH1}\right) / I_{ave,pHn-after} \tag{6}$$

where $I_{ave,pH1}$ is the average photocurrent measured (during the 2 min interval) when the PANI-based film was treated with the pH 1 buffer solution and on top of the P3HT:PCBM-based film, $I_{ave,pHn}$ is the same but for the PANI-based film treated with a pH *n* buffer solution (*i.e.*, *n* ranges from pH 1 to 13), and $I_{ave,pHn-after}$ is the average photocurrent measured immediately after pH *n* buffer treatment and without the PANI-based film. Figure 13 summarizes a representative test result and also includes data from films interrogated using blue light and near-IR light. From figure 13, it is obvious that the pH sensitivity of the film, when excited using blue light, is close to zero and does not possess a strong trend. The film's poor pH performance using a blue light source (*i.e.*, 450±40 nm BP filter) is a favorable response, since excellent strain sensitivity have been observed and reported in sections 4.4 and 4.5. It should be noted that the normalized change in photocurrent shown in figure 13, when interrogated by blue light, is still on the order of 1 to 2%. In order to resolve the film's strain response (see figures 10a and 11a), the assumption is that the sensor needs to be exposed to a nearly constant pH environment. From a structural health monitoring perspective, this assumption is acceptable since corrosion usually occurs over long time-scales, as compared to strain due to structural loading, impact, or cracking.

In contrast, when using near-IR light, strain sensitivity is suppressed (section 4.4), but figure 13 confirms high pH sensitivity. In fact, pH sensitivity is especially dramatic in the pH range from 4 to 11 where large changes in photocurrent have been measured. This result is expected, since section 3.3 has already showed that the PANI-based film's optical transmittance increases from ~15% to ~60% as pH increases from 1 to 13 (*i.e.*, see figure 6b and for light wavelengths >800 nm). Although the magnitude of DC photocurrent is low (especially compared to the blue light excitation), the dramatic change in photocurrent makes pH sensing possible. In particular, given the noise floor of the film's near-IR photocurrent response shown in figure 10b, pH sensing is likely to be most reliable in the pH range from 5 to 11. Sensing resolution will depend on the resolution of the current measurement hardware, as well as

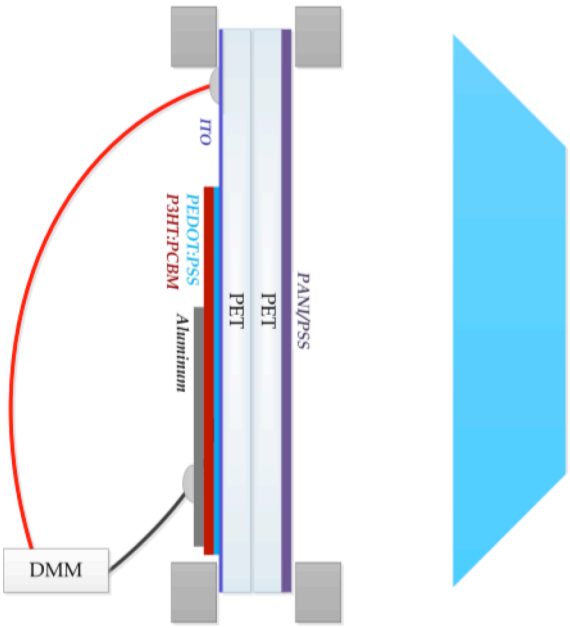

Figure 14. A multilayered thin film sensor was prepared by integrating the P3HT:PCBM-ITO/PET specimen with a 20 bilayer LbL PANI/PSS-ITO specimen. The multilayered film was mounted onto the load frame for conducting strain sensing validation tests in which the film was interrogated by blue light and subjected to various pH levels.

the film's noise floor (which is not characterized in this study). Based on the results presented in this section, it is also apparent that near-IR light is suitable for selective pH sensing.

4.7 pH Effects on Strain Sensing

Considering that strain and pH sensing is to be realized simultaneously and on a single sensing platform, it is necessary to characterize the strain sensing response of P3HT:PCBM-ITO/PET specimens while PANI/PSS-PET films are also exposed to various pH levels. It should be mentioned that, it is not necessary to investigate the effects of strain on the integrated sensor's pH response. Previous results have already demonstrated that photocurrent generated by IR light illumination is insensitive to strain as shown in figure 10b.

A multilayered thin film sensor was prepared by integrating the #5 P3HT:PCBM-ITO/PET specimen with a 20-bilayer LbL PANI/PSS-PET specimen. As shown in figure 14, the multilayered film was mounted in the Test Resources 150R load frame. A total of five sets of strain sensing tests were conducted, where each set involved treating the sensor to a certain pH buffer solution (*i.e.*, pH 1, 4, 7, 10, and 13). A sixth test was also performed as a reference, where the P3HT:PCBM-ITO/PET specimen was tested without the incorporation of the PANI-based film. The testing protocol followed the same procedure described in section 4.4. Again, blue light was employed for interrogating the sensor's strain response.

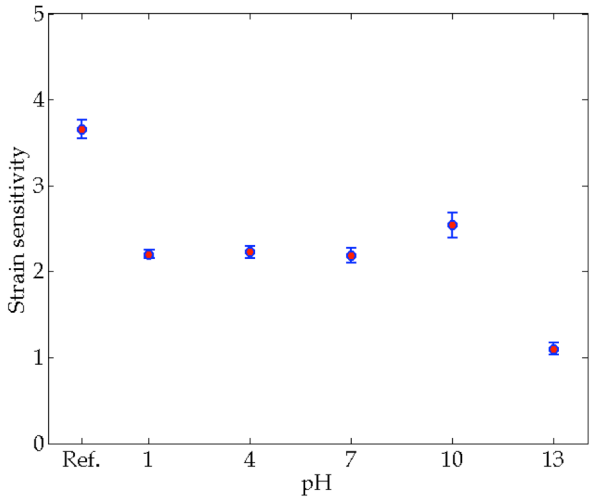

Figure 15. The strain sensitivities of the integrated sensor were obtained and plotted with respect to five different pH levels that the sensor was treated with. A reference or control specimen without integrating the PANI-based film was also tested and the results included for comparison.

To compare the multilayered thin film's strain sensing properties at various pH levels, the average strain sensitivities and corresponding standard errors of the mean were calculated and plotted in figure 15. First, compared to the reference, it has been found that strain sensitivity for the integrated sensor decreased after incorporation of the LbL PANI/PSS film. This decrease in strain sensitivity occurs because it has been found that the optical transmittance of the PANI/PSS thin film exhibits a slight sensitivity to applied tensile strains [42]. In particular, UV-Vis results showed that PANI/PSS film's light transmittance at 450 nm were inversely but linearly correlated to strain (*i.e.*, negative strain sensitivity) [42]. Despite this decrease in strain sensitivity, figure 15 clearly shows that the integrated thin film still demonstrates consistent strain sensitivity at different pH levels. The only exception is test results corresponding to the pH 13 case. This test case was also the last among all the tests conducted, and it is suspected that the PANI/PSS films may have been damaged after repeated testing. Nevertheless, the results presented in figure 15 confirm multi-modal sensing.

5. Conclusions

Structural failure is often triggered by simultaneously occurring yet different types of damage. In particular, cracks and corrosion are two of the most common and serious damage that could occur in civil, mechanical, naval, and aerospace structures. In this work, a multi-modal, photoactive, and self-sensing thin film is demonstrated for sensing strain (*i.e.*, cracks) and pH (or corrosion). The photoactive thin film generates DC current due to light illumination, and the generated current is used directly as the sensing signal. Its ability to generate stimuli-sensitive electrical current makes this material unique and self-sensing. A multi-layered film architecture is employed for achieving multi-modal sensing.

First, spin-coated P3HT:PCBM films deposited onto ITO-PET substrates form the photoactive and strain-sensitive layer. The P3HT:PCBM thin film forms a p-n BHJ structure, and photonic energy

(*i.e.*, illuminated light) can be converted to electrical energy (*i.e.*, DC photocurrent). Previous work has shown that photocurrent generated by broadband light illumination is also sensitive to applied strains. This study extends previous work by characterizing their optical or UV-Vis response to applied strains. It has been found that, in the range from 400 to 650 nm, P3HT:PCBM light absorption varies linearly with strain. Second, pH or corrosion sensitivity has been encoded using PANI-based thin films. A layer-by-layer assembly method has been employed for fabricating thin films deposited on glass and PET substrates. The UV-Vis properties of PANI-based films treated with pH 1 to 13 buffer solutions have also been characterized. It has been shown that the film's light transmittance greater than 800 nm (*i.e.*, in the near-IR range) is extremely sensitive to pH. Transmittance increases from ~15% for pH 1 to ~60% for pH 13.

Lastly, multi-modal strain and pH sensing using the proposed thin film sensor has been validated. By shining blue light (*i.e.*, after equipping a solar simulator with AM 1.5G and 450±40 nm band-pass filters), the film has been validated for generating strain-sensitive photocurrent. The film has been demonstrated to measure tensile strains up to 5,000 με or 0.5% and over repeated cycles of loading. Its average strain sensitivity (or gage factor) is calculated to be ~3.2. However, strain sensitivity is affected by loading rate and decreases with increasing load rates. In addition, it has been shown that the integration of the PANI-based film decreased strain sensitivity of the multi-modal thin film sensor. On the other hand, near-IR light has been used for interrogating these films and has been validated to successfully generate pH-sensitive photocurrent. The sensitivity to pH has been particularly dramatic in the range from pH 5 to 11. Future work will entail sensor performance optimization, the encoding of other different sensing functionalities, and extensive testing in more realistic operating conditions.

Acknowledgements

The authors thank the National Science Foundation (NSF) for supporting this research, under grant no. CMMI-1031754. Additional financial support has also been provided by the College of Engineering and the University of California-Davis Humanities Graduate Research Award. The authors would also like to thank Mr. Baptiste Josse and Mr. Frederick Meyers for their assistance with experimental preparation, testing, and data collection.

References

[1] Biezma M and Schanack F 2007 Collapse of steel bridges *J. Perform. Constr. Facil.* **21** 398-405
[2] Peekema R 2013 Causes of natural gas pipeline explosive ruptures *J. Pipeline Syst. Eng. Pract.* **4** 74-80
[3] Pitt S and Jones R 1997 Multiple-site and widespread fatigue damage in aging aircraft *Eng. Failure Anal.* **4** 237-257
[4] Kay J *The columbia space shuttle disaster: Science and the profit system-part 1: The physical cause of the accident and the decay of shuttle infrastructure, 03 October 2013*(World Socialist Web Site, 2003)
[5] United States. National Transportation Safety B *Natural gas pipeline rupture and fire near Carlsbad, New Mexico* (National Transportation Safety Board, Washington, D.C., 2003)

[6] Achenbach J 2000 Quantitative nondestructive evaluation *Int. J. Solids Struct.* **37** 13-27
[7] Rakow A and Chang F-K 2012 A structural health monitoring fastener for tracking fatigue crack growth in bolted metallic joints *Struct. Health Monit.* **11** 253-267
[8] Xu X and Huang H 2012 Multiplexing passive wireless antenna sensors for multi-site crack detection and monitoring *Smart Mater. Struct.* **21** 015004
[9] Minakuchi S, Yamauchi I, Takeda N and Hirose Y 2012 Memorizing and detecting an arrested crack in a foam-core sandwich structure using embedded plastic materials and fiber-optic sensors *Smart Mater. Struct.* **21** 055025
[10] Terasaki N, Chenshu L, Lin Z and Chao-Nan X, Active crack indicator with mechanoluminescent sensing technique: Detection of crack propagation on building *Sensors Applications Symposium (SAS), 2012 IEEE*, 2012
[11] Withey P A, Vemuru V S M, Bachilo S M, Nagarajaiah S and Weisman R B 2012 Strain paint: Noncontact strain measurement using single-walled carbon nanotube composite coatings *Nano Lett.* **12** 3497-3500
[12] Weisman R B, Withey P A, Bachilo S M, Nagarajaiah S and Vemuru V S M, US Patent No. WO 2013/184212 A2 (2013).
[13] Sohn H-G, Lim Y-M, Yun K-H and Kim G-H 2005 Monitoring crack changes in concrete structures *Copmut. Aided Civil Infrastruct. Eng.* **20** 52-61
[14] He Y, Tian G, Zhang H, Alamin M, Simm A and Jackson P 2012 Steel corrosion characterization using pulsed eddy current systems *IEEE Sens. J.* **12** 2113-2120
[15] Yu L, Giurgiutiu V, Wang J and Shin Y-J 2012 Corrosion detection with piezoelectric wafer active sensors using pitch-catch waves and cross-time–frequency analysis *Struct. Health Monit.* **11** 83-93
[16] Vandenberg A and Loh K J 2012 Evaluating the pH sensitivity of carbon nanotube-polyaniline thin films with different dopants *Nano LIFE* **02** 1242001
[17] Lee D and Cui T 2012 Carbon nanotube thin film pH electrode for potentiometric enzymatic acetylcholine biosensing *Microelectron. Eng.* **93** 39-42
[18] Kaempgen M and Roth S 2006 Transparent and flexible carbon nanotube/polyaniline pH sensors *J. Electroanal. Chem.* **586** 72-76
[19] Jin Z, Su Y and Duan Y 2000 An improved optical pH sensor based on polyaniline *Sensors Actuators B: Chem.* **71** 118-122
[20] Lin J and Liu D 2000 An optical pH sensor with a linear response over a broad range *Anal. Chim. Acta* **408** 49-55
[21] Lin J 2000 Recent development and applications of optical and fiber-optic pH sensors *TrAC, Trends Anal. Chem.* **19** 541-552
[22] Pringsheim E, Terpetschnig E and Wolfbeis O S 1997 Optical sensing of pH using thin films of substituted polyanilines *Anal. Chim. Acta* **357** 247-252
[23] Grummt U-W, Pron A, Zagorska M and Lefrant S 1997 Polyaniline based optical pH sensor *Anal. Chim. Acta* **357** 253-259
[24] de Marcos S and Wolfbeis O S 1996 Optical sensing of pH based on polypyrrole films *Anal. Chim. Acta* **334** 149-153
[25] Tsai Y-T, Wen T-C and Gopalan A 2003 Tuning the optical sensing of pH by poly(diphenylamine) *Sensors Actuators B: Chem.* **96** 646-657
[26] Loh K J, Kim J, Lynch J P, Kam N W S and Kotov N A 2007 Multifunctional layer-by-layer carbon nanotube–polyelectrolyte thin films for strain and corrosion sensing *Smart Mater. Struct.* **16** 429
[27] Zhang W, Suhr J and Koratkar N 2006 Carbon nanotube/polycarbonate composites as multifunctional strain sensors *J. Nanosci. Nanotechnol.* **6** 960-964
[28] Ryu D and Loh K J 2012 Strain sensing using photocurrent generated by photoactive P3HT-based nanocomposites *Smart Mater. Struct.* **21** 065016
[29] Ryu D and Loh K J 2013 Analyzing the strain sensing response of photoactive thin films using absorption spectroscopy *Key Eng. Mater.* **569-570** 695-701
[30] Li G, Zhu R and Yang Y 2012 Polymer solar cells *Nature Photon.* **6** 153-161

[31] Ren S, Bernardi M, Lunt R R, Bulovic V, Grossman J C and Gradečak S 2011 Toward efficient carbon nanotube/P3HT solar cells: Active layer morphology, electrical, and optical properties *Nano Lett.* **11** 5316-5321
[32] Skotheim T A, Elsenbaumer R L and Reynolds J R *Handbook of conducting polymers* (Marcel Dekke, Inc., New York, NY, 1998)
[33] O'Connor B, Kline R J, Conrad B R, Richter L J, Gundlach D, Toney M F and DeLongchamp D M 2011 Anisotropic structure and charge transport in highly strain-aligned regioregular poly(3-hexylthiophene) *Adv. Funct. Mater.* **21** 3697-3705
[34] Bhadra S, Khastgir D, Singha N K and Lee J H 2009 Progress in preparation, processing and applications of polyaniline *Prog. Polym. Sci.* **34** 783-810
[35] Decher G and Schlenoff J *Multilayer thin films* (WILEY-VCH Verlag GmbH & Co. KGaA, Weinheim, 2006)
[36] Wu Z, Song T, Jin Y and Sun B 2011 High performance solar cell based on ultra-thin poly(3-hexylthiophene): Fullerene film without thermal and solvent annealing *Appl. Phys. Lett.* **99** 143306-143303
[37] Chu C-W, Yang H, Hou W-J, Huang J, Li G and Yang Y 2008 Control of the nanoscale crystallinity and phase separation in polymer solar cells *Appl. Phys. Lett.* **92** 103306-103303
[38] Kim Y, Cook S, Tuladhar S M, Choulis S A, Nelson J, Durrant J R, Bradley D D C, Giles M, McCulloch I, Ha C-S and Ree M 2006 A strong regioregularity effect in self-organizing conjugated polymer films and high-efficiency polythiophene:Fullerene solar cells *Nat. Mater.* **5** 197-203
[39] Erb T, Zhokhavets U, Gobsch G, Raleva S, Stühn B, Schilinsky P, Waldauf C and Brabec C J 2005 Correlation between structural and optical properties of composite polymer/fullerene films for organic solar cells *Adv. Funct. Mater.* **15** 1193-1196
[40] Ryu D and Loh K J, Characterizing the self-sensing properties of photoactive P3HT-based nanocomposites *2013 9th International Workshop on Structural Health Monitoring (IWSHM)*, Stanford, CA, 2013
[41] Goutam P J, Singh D K, Giri P K and Iyer P K 2011 Enhancing the photostability of poly(3-hexylthiophene) by preparing composites with multiwalled carbon nanotubes *J. Phys. Chem. B* **115** 919-924
[42] Ryu D and Loh K J, Photoactive and self-sensing P3HT-based thin films for strain and corrosion monitoring *SPIE 2014 Conference on Sensors and Smart Structures Technologies for Civil, Mechanical, and Aerospace Systems*, San Diego, CA, 2014